The Astrophysical Journal, 681:650–663, 2008 July 1
© 2008. The American Astronomical Society. All rights reserved. Printed in U.S.A.

HELIUM LINE FORMATION AND ABUNDANCE DURING A C-CLASS FLARE

Vincenzo Andretta
INAF-Osservatorio Astronomico di Capodimonte, Salita Moiariello 16, I-80131 Napoli, Italy; andretta@oacn.inaf.it

Pablo J. D. Mauas
Instituto de Astronomía y Física del Espacio, Argentina

Ambretta Falchi
INAF-Osservatorio Astrofisico di Arcetri, Italy

and

Luca Teriaca
Max-Planck-Institut für Sonnensystemforschung, Germany
Received 2007 December 14; accepted 2008 February 29

ABSTRACT

During a coordinated campaign that took place in 2001 May, a C-class flare was observed both with *SOHO* instruments and with the Dunn Solar Telescope of the National Solar Observatory at Sacramento Peak. In two previous papers we described the observations and discussed some dynamical aspects of the earlier phases of the flare, as well as the helium line formation in the active region prior to the event. Here we extend the analysis of the helium line formation to the later phases of the flare in two different locations of the flaring area. We have devised a new technique, exploiting all available information from various *SOHO* instruments, to determine the spectral distribution of the photoionizing EUV radiation produced by the corona overlying the two target regions. In order to find semiempirical models matching all of our observables, we analyzed the effect on the calculated helium spectrum, both of $A_{\rm He}$ (the He abundance) and of the uncertainties in the incident EUV radiation (level and spectral distribution). We found that the abundance has in most cases (but not in all) a larger effect than the coronal back-radiation. The result of our analysis is that, considering the error of the measured lines and adopting our best estimate for the coronal EUV illumination, the value $A_{\rm He} = 0.075 \pm 0.010$ in the chromosphere (for $T > 6300$ K) and transition region yields reasonably good matches for all the observed lines. This value is marginally consistent with the most commonly accepted photospheric value, $A_{\rm He} = 0.085$.

Subject headings: Sun: abundances — Sun: activity — Sun: chromosphere

1. INTRODUCTION

A key ingredient to understanding the physics of solar and stellar plasmas is their chemical composition. An astrophysical plasma is subject to chemical fractionation processes of diverse nature (gravity, thermal diffusion, etc.; see, e.g., Drake 2003) that can produce abundance anomalies between regions of different temperature and density. For the solar corona, these anomalies are generally described in terms of the so-called FIP (first ionization potential) effect. Not only the details, but the very general physical framework behind this effect is still debated. However, one of the few aspects over which there is apparently a consensus is that the FIP effect should arise in the chromosphere (Geiss 1982, 1998).

Helium is one of the few elements that exhibits strong lines forming in the chromosphere, and thus, in principle at least, its abundance ($[{\rm He/H}] \equiv \log A_{\rm He}$, where $A_{\rm He} \equiv N_{\rm He}/N_{\rm H}$, the ratio of number densities of He and H), could be estimated in that region. It is also the element with the highest FIP (24 eV). Furthermore, it is the second most abundant element in the Sun (and in the universe, for that matter) and therefore must be included in any theoretical model of fractionation processes in the solar atmosphere. Moreover, the coronal [He/H] strongly depends on the availability of helium in the upper chromosphere (e.g., Killie et al. 2005).

Unfortunately, analyzing helium lines in the solar atmosphere is a particularly challenging task, more so than other typical chromospheric lines, such as Hα or the Ca II H and K doublet. The main reasons are described in several papers (e.g., Andretta & Jones 1997; Pietarila & Judge 2004). Among the problems that can be mentioned, all of its lines need detailed radiative transfer calculations, strong interlocking between the $n = 2$ and 3 singlet and triplet levels makes the *simultaneous* treatment of EUV and optical lines almost unavoidable, the high excitation energies of all helium lines (a consequence of its high FIP value) makes those lines very sensitive to nonequilibrium effects, the ionization rates of neutral and ionized helium can be significantly affected by EUV radiation via the so-called photoionization-recombination (P-R) mechanism (e.g., Zirin 1975; Andretta et al. 2003), and therefore not only coronal plasmas, but even the strong He II Lyα at 30.4 nm can be significant photoionization sources for neutral helium (another example of the strong interlocking effects in the helium atomic system).

All these problems imply, among other things, that a realistic study of helium lines in the solar chromosphere requires quite sophisticated modeling, as well as simultaneous measurements in both the EUV and the optical (visible and IR) range. To this aim we planned an observing campaign (*Solar and Heliospheric Observatory* [*SOHO*] Joint Observing Program 139) coordinated between ground-based and *SOHO* instruments to obtain simultaneous spectroheliograms of the same area in several spectral lines, including four He lines (He I 587.6 nm, He I 1083.0 nm, He I 58.4 nm, and He II 30.4 nm), that sample the solar atmosphere from the chromosphere to the transition region. The EUV radiation

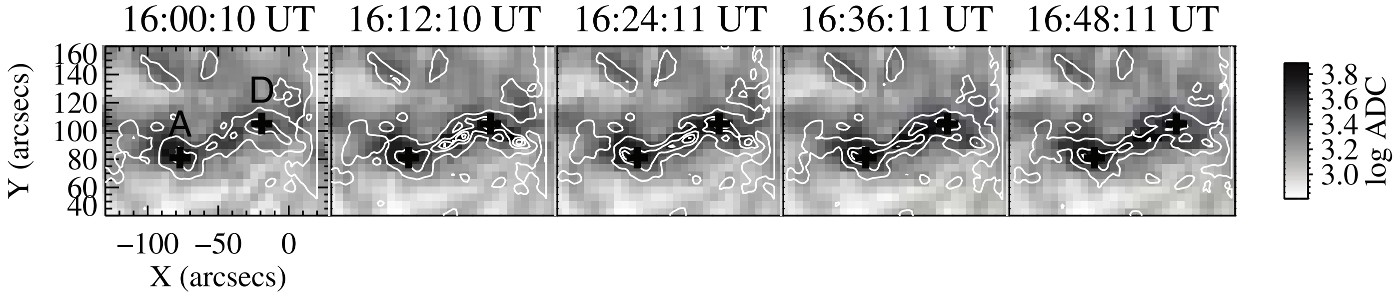

Fig. 1.—Evolution of the NOAA AR 9468 in the first hour of the event, as seen in the sequence of *SOHO* EIT 19.5 nm images (see Fig. 2 for a comparison with EUV and soft X-ray irradiance and Hα radiance light curves). The contours represent Hα isophotes relative to the DST raster scan nearest in time. The positions of the two regions studied in detail in this paper (regions A and D) are marked with crosses.

in the ranges $\lambda < 50$ nm and 26 nm $< \lambda <$ 34 nm was also measured at the same time.

In a previous paper (Mauas et al. 2005, hereafter Paper II), we carried out an analysis of the helium line formation in a specific location of the observed active region (NOAA AR 9468, $\cos\theta = 0.99$) prior to a small two-ribbon flare (*Geostationary Operational Environmental Satellite* [*GOES*] class C1) that developed in this region on 2001 May 26, around 16:00 UT. We found that the incident coronal radiation has a limited effect on the UV He lines (in partial agreement with the proxy-based analysis of Fredvik & Maltby 1999 of the He i 58.4 nm line), while being fundamental for the optical lines. For these lines, we also found that photons of shorter wavelengths are more effective at increasing their line depth. Incidentally, this latter finding implies that for the calculation of the He line profiles it is important, at least in principle, to correctly estimate not only the total number of ionizing photons, but also their spectral distribution. But the main result of Paper II was that the photospheric value of [He/H] is compatible with our observations within an uncertainty of about a factor of 2 and that such uncertainty could be reduced in a higher density regime.

On the basis of these results, we decided to extend our analysis to the data taken during the flare. In this paper we present results of such an analysis and study the formation of He lines after the main evaporation phase, when the He lines presumably originate in a high-density plasma, and the incident coronal radiation, larger than in the preflare phase, can be estimated with a lower uncertainty. We construct semiempirical models of the flaring atmosphere to match the observed line profiles from the chromosphere to the transition region, taking into account the total EUV irradiance in the range $\lambda < 50$ nm. We also analyze the effect of [He/H] changes, with the purpose of attaining an empirical estimate of that parameter.

In this regard, we mention that techniques based on γ-ray line measurements produced in flares offer an alternative avenue for estimating the chromospheric He abundance (e.g., Mandzhavidze et al. 1997, 1999; Share & Murphy 1998). Results from these techniques seem generally to indicate an enhancement either of the accelerated α/proton ratio or of the ambient He abundance. Attempts to resolve this ambiguity seem, however, to hint that $A_{\rm He}$ is consistent with its accepted photospheric values (Murphy 2007).

For completeness, we should also mention recent EUV spectroscopic measurements of $A_{\rm He}$ during a flare, made by analyzing the Baγ of He ii at 108.5 nm in off-limb spectra (Feldman et al. 2005), which yielded $A_{\rm He} \sim 0.122 \pm 0.024$, marginally higher than the photospheric value. This result, however, refers to off-limb postflare loops and thus cannot be directly compared with our on-disk, chromospheric measurements.

In § 2 we briefly describe the set of observations, focusing our attention on two specific locations of the flaring region. In § 3 we describe the procedures employed to estimate the incident coronal EUV radiation illuminating the regions under examination and in § 4 the chromospheric modeling for those two locations. Finally, in § 5 we explore how the helium spectrum is affected by the value of the chromospheric He abundance and by the uncertainties in the estimates of coronal radiation.

2. THE OBSERVATIONS

A detailed description of the observing program is given in Teriaca et al. (2003, hereafter Paper I). We recall here that spectroheliograms were acquired with the Horizontal Spectrograph at the Dunn Solar Telescope (DST) of the National Solar Observatory at Sacramento Peak in the chromospheric lines Ca ii K, Hα, and Na i D, as well as in the He i lines at 587.6 nm (D_3) and 1083 nm. The full field of view (FOV) of the DST, $170'' \times 170''$, was covered in about 5 minutes, with a sampling step of 2″. Correcting for offsets among the different detectors resulted in a final useful FOV of $160'' \times 140''$ with an effective resolution of 2″.

During the same period, spectroheliograms of the active region were obtained in selected spectral lines with the Normal Incidence Spectrometer (NIS) of the Coronal Diagnostic Spectrometer (CDS; Harrison et al. 1995) aboard *SOHO*. The selected lines are Fe xvi 36.1 nm in the NIS band 1; He i 58.4 nm, He ii 30.4 nm (second order), O v 62.9 nm, and the blend Fe xii 59.26 + Fe xix 59.22 nm[1] in the NIS band 2. The 4″ wide slit was stepped 6″, covering a 148″ wide area in ~5.5 minutes. The final useful FOV was $148'' \times 138''$ with an effective pixel size of $6'' \times 3.4''$. Ground-based and CDS data were aligned using *SOHO* MDI images as a reference. We estimate the error as around a few arcseconds. CDS and ground-based spectra are simultaneous within 2 minutes.

Another *SOHO* instrument, the Extreme ultraviolet Imaging Telescope (EIT; Delaboudinière et al. 1995), provided synoptic series of full-disk images centered on 17.1, 19.5, 28.4, and 30.4 nm around 13:00 and 19:00 UT, plus a series of full-disk images centered on 19.5 nm acquired with a 12 minute cadence during the routine CME watch program. Figure 1 shows a few images extracted from the EIT 19.5 sequence, showing the development of the flare.

Finally, the EUV flux during the flare (see Fig. 2) was observed by the Solar EUV Monitor (SEM) instrument aboard *SOHO* (Hovestadt et al. 1995). The CELIAS SEM instrument provides calibrated total photon counts in the ranges $\lambda < 50$ nm

---

[1] In the case of the Fe xii 59.26 + Fe xix 59.22 nm blend, an analysis of the mean line wavelengths shows (see also Paper I) that the former contribution is small or even negligible in the areas interested by the flare, but, conversely, is dominant in the surrounding, unperturbed regions.

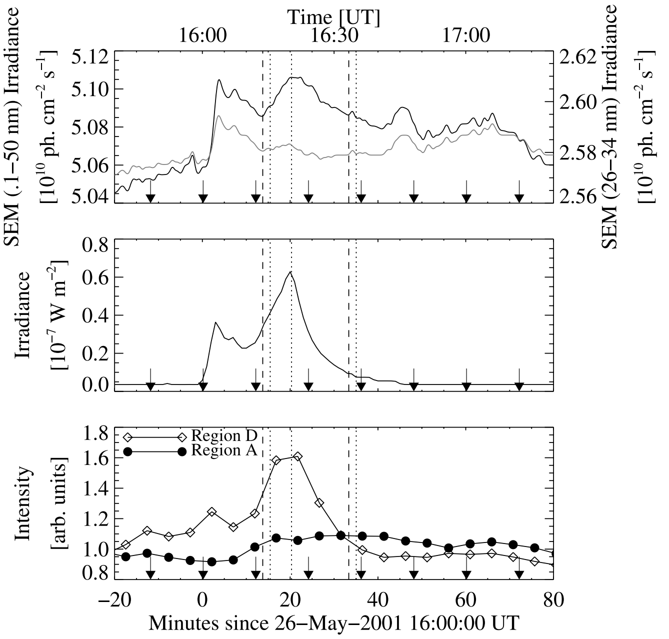

FIG. 2.—Light curves in the EUV and soft X bands (1 minute resolution), before and during the C-class flare studied in this paper, compared with optical measurements. *Top*: EUV Irradiance at 1 AU, from *SOHO* SEM (*black*: $\lambda < 50$ nm; *gray*: 26 nm $< \lambda <$ 34 nm). *Middle*: Soft X irradiance from *GOES-10* (0.05–0.4 nm band). *Bottom*: Hα intensity observed at the Dunn Solar Telescope (DST) in the two representative regions analyzed in this paper (see Fig. 1). The vertical arrows mark the times of the full-disk images in the 19.5 nm band taken by *SOHO* EIT during the CME watch observing program, while the vertical dashed and dotted lines mark the times of the spectra of regions A and D, respectively.

(zeroth order, SEM$_{[0]}$) and 26 nm $< \lambda <$ 34 nm (first order, SEM$_{[1]}$) at 1 AU.

The flare dynamics has been discussed in Paper I, where it has been shown that a large area of the flaring region is affected by chromospheric evaporation in a short time interval (16:02:30–16:05:30 UT) during the first impulsive phase. In the present paper we analyze the He line profiles after 16:13 UT, when the chromospheric evaporation is almost finished, in two distinct locations, which we term regions A and D (size $4'' \times 2''$ each). These two regions are marked in Figure 1.

From what we obtained in Paper I, region A did not undergo any evaporation process, at least within our limit of detectability, while region D is in the area where we measured downflows at chromospheric levels and upflows at transition region (TR) and coronal levels. Moreover, while in region A the chromospheric radiance is almost constant after 16:13 UT, in region D it approximately follows the EUV light curve (see Fig. 2), with a secondary maximum at about 16:20 UT, showing that this small flare is also a multiple event. A similar behavior is also detected for the TR and coronal lines with temperatures up to 10^6 K.

We use region A as a control region where only small changes are detected in our observed features. We construct (§ 4) semi-empirical models of the flaring atmosphere for this region at two times when the SEM EUV irradiance is nearly the same, 16:14 and 16:33 UT (Fig. 2, *top*, *dashed lines in the SOHO SEM light curve*).

For region D the models are constructed at 16:15, 16:20, and 16:35 UT (Fig. 2, *top*, *dotted lines*). These times are also referred to as t_1, t_2, and t_3, respectively. Time t_2 corresponds to a peak of the total SEM irradiance, while at t_1 and t_3 the irradiances are almost equal. Therefore, the choice of these regions and times allows us to check whether and how the He I lines are influenced by the EUV coronal back-radiation and/or by the atmosphere where they form. This point is discussed in more detail in § 3.1.

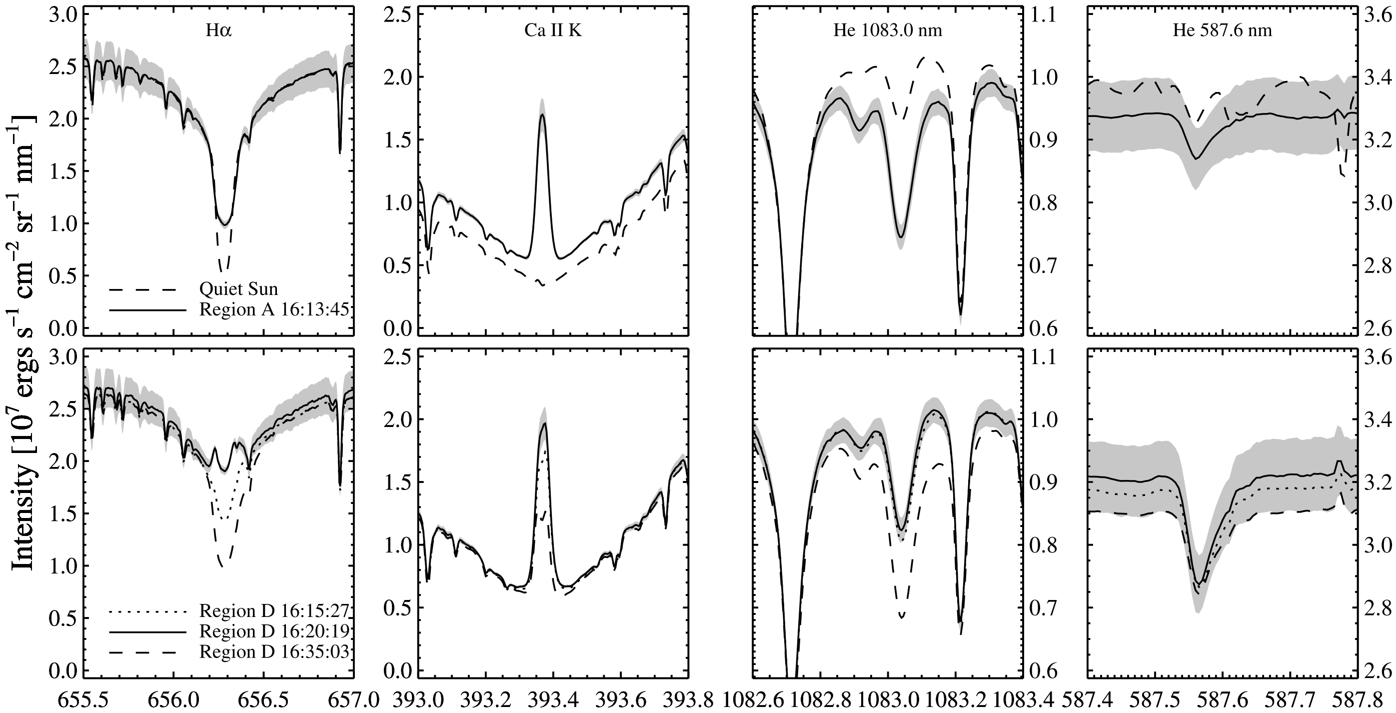

FIG. 3.—Profiles for the lines Hα, Ca II K, and He I 1083.0 and 587.6 nm. *Top*: Observations in a quiescent reference region (*dashed lines*) and in region A at 16:14 UT (*solid lines*). *Bottom*: Observations in region D at 16:15 (*dotted lines*), 16:20 (*solid lines*), and 16:35 UT (*dashed lines*). Error bands for the profiles in region A at 16:14 UT and region D at 16:20 UT are also shown. Note that telluric lines have been removed from the He I 587.6 nm profiles, except in the case of the reference region.

The two sets of optical line profiles are shown in Figure 3, with the exception of the Na I doublet, which did not change during the flare in the two considered regions. For region A, since the profiles remain practically unchanged, only the profiles observed at 16:14 are shown and compared with profiles taken in a nearby, relatively quiescent region, prior to the flare, which have been used to calibrate the spectra in absolute units.

The noise of individual spectra is sufficiently small to be negligible compared to the pixel-to-pixel variability within the target regions that, therefore, determines the uncertainty on the mean profiles. The uncertainties as a function of wavelength on the mean profiles in region A at 16:14 UT and in region D at 16:20 UT are indicated in Figure 3 as a gray band. In practice, those bands are obtained at each wavelength from the rms of the N profiles within the target regions divided by $\sqrt{N}$.

It is important to realize that for the two relatively weak He I lines, the uncertainty in the central line depth (the quantity that carries most information about the chromosphere) is also due to the variability of the underlying photosphere. This fact is most evident in the continuum bands of the D_3 line at 587.6 nm. By examining the variability of the profiles normalized to the continuum, we estimate that for the latter line the photospheric variability contributes by about 50% to the variability of the central line intensity.[2] In any case, the uncertainties shown in Figure 3 for the two optical He I lines (of the order of 3%) are to be taken as upper limits for the uncertainties due to the variability of the chromosphere only.

In the case of the EUV He I lines, the width of the instrumental response of the CDS spectrograph prevents a detailed comparison of computed and observed line profiles. We thus considered only the radiances. For these lines, the main source of error is the uncertainty in the absolute radiometric calibration, estimated to be of the order of 30%.

3. CORONAL BACK-RADIATION

In Paper II the average EUV illumination over the target area in active region AR 9468, integrated in the $\lambda < 50$ nm range, was computed using the spatial information provided by the EIT synoptic images to estimate the contribution to the full-disk $\mathrm{SEM}_{[0]}$ 0.1–50 nm irradiance due to the target region. This value, $I_{\mathrm{ref}} = (1.2 \pm 0.2) \times 10^{15}$ photons $\mathrm{s^{-1}\ cm^{-2}\ sr^{-1}}$, is considered here as the reference value. We recall that the emission from the He II lines has been subtracted from I_{ref} because these lines are taken into account in a self-consistent way in the model computations.

Following the same approach and using the EIT 19.5 images as proxies, we estimated that in the hour before the flare the EUV radiation in regions A and D was on average about 2.2 and 1.6 times higher than I_{ref}. Since there are variations of the order of 30% in a 3×3 pixel box ($\approx 16'' \times 16''$) around the center of each region, the standard deviation of the *mean* value in the same box would be 3 times smaller. We, however, prefer to use the 3 σ value on the mean value quoted above, as it is large enough to encompass other possible sources of error (for instance, those introduced by the use of EIT 19.5 images as proxies for the full 1–50 nm range). Thus, we estimated the EUV illumination over regions A and D to be, respectively, about 2.6×10^{15} and 1.9×10^{15} photons $\mathrm{s^{-1}\ cm^{-2}\ sr^{-1}}$ (Table 1).

TABLE 1

CORONAL RADIANCES FOR REGIONS A AND D

TIME (UT)	CORONAL RADIANCE		
	Excess	Total	Total / I_{ref}
Region A			
Preflare	. . .	2.6	2.2
16:14	0.38	3.0	2.5
16:33	1.73	4.4	3.6
Region D			
Preflare	. . .	1.9	1.6
16:16	5.48	7.3	6.2
16:20	7.38	9.2	7.7
16:35	5.25	7.1	6.0

NOTES.—Units are 10^{15} photons $\mathrm{s^{-1}\ cm^{-2}\ sr^{-1}}$. The value $I_{\mathrm{ref}} = 1.2 \times 10^{15}$ is the reference (average preflare) value for the target area, estimated in Paper II.

The implicit assumption in such an approach, as explained in Paper II, is that the spectral distribution of the EUV radiation over the active region does not change significantly. For the observations taken during the flare, however, this assumption may not be valid. Thus, we adopted an altogether different approach for estimating the EUV illumination at the times of our observations.

From the EIT sequence of images, we can estimate that the only event that could cause the increase in EUV irradiance shown in the topmost panel of Figure 2 is the C-class flare that we observed. From the increase in SEM irradiance, Δf, and from the knowledge of the angular area affected by the flare, $\Delta\Omega$, we can then estimate the increase in radiance in the flaring region, $\Delta I = \Delta f / \Delta\Omega$. The total radiance in the region is then obtained by adding to ΔI the estimates of the preflare average radiances given above.

For a first, rough estimate, we can start from a visual determination, from Figure 2, of the excess irradiance in the $\mathrm{SEM}_{[0]}$ measurements due to that event, $\Delta f \approx 2$ to 4×10^8 photons $\mathrm{s^{-1}\ cm^{-2}}$ in the first 60 minutes of the event. On the other hand, from both EIT and CDS observations, we estimate flare areas to be of the order of $\Delta\Omega \approx 1500$–$2000$ arcsec^2 in the same time interval. Consequently, we expect radiances in the flaring regions to increase by something of the order of $\Delta I \approx 6$ to 8×10^{15} photons $\mathrm{s^{-1}\ cm^{-2}\ sr^{-1}}$.

The inaccuracy of this estimate is mainly due to the approximate definition of the flaring area: it can vary by as much as a factor of 2 or 3, depending on which spectral signature is considered. For a more precise determination of the excess irradiances in regions A and D, we refined the method by using the information given by the variation in time (light curves) *above the preflare mean value* of both the SEM irradiance and of the observed spectral signatures in our data set. In more detail, we proceeded as follows:

Step 1. We created a set of reference images, both from CDS and from EIT, by averaging the (co-aligned) images in the 40 minutes preceding the onset of the event. The variability of these images around the average is of the order of 0.1%–0.2% (standard deviation) or even less.

Step 2. We obtained maps of residual or excess radiance in each spectral feature during the flare, $\Delta I_{ij}^{k}(t_h)$, by subtracting the reference preflare images (taking into account solar rotation) for each time t_h and for each pixel (i, j). Multiplying by the pixel angular size, $d\omega^k$, we then obtain the contribution of each line

---

[2] We adopt here, as is commonly done in astrophysics, the term "specific intensity" or simply "intensity" in place of the more formally correct "spectral radiance" (SI units: W $\mathrm{sr^{-1}\ m^{-2}\ nm^{-1}}$) and indicate it with the symbol I_λ; "radiance" then means an intensity integrated over a wavelength band or a line profile: $\int I_\lambda \, d\lambda$ (SI units: W $\mathrm{sr^{-1}\ m^{-2}}$). Finally, "irradiance" is the spectral and angular integral of an intensity: $\int I_\lambda \, d\lambda \, d\Omega$ (SI units: W $\mathrm{m^{-2}}$).

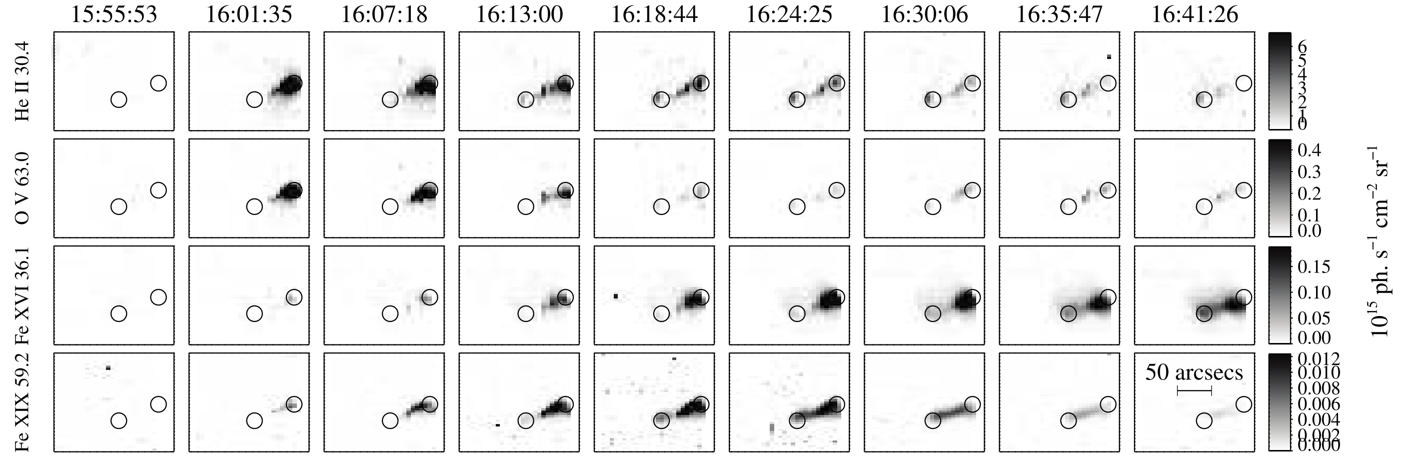

FIG. 4.—Sequences of CDS NIS *residual* spectroheliograms showing, for about 40 minutes, the evolution of the event from its onset (at about 16:01 UT). The images obtained from the profiles of the He I 58.4 nm line are very similar to those of the He II 30.4 nm line and thus are not shown here. Circles mark the two regions of interest (A and D: leftmost and rightmost circles, respectively).

and each pixel to the EUV irradiance, $\Delta f_{ij}^k(t_h) = \Delta I_{ij}^k(t_h)\,d\omega^k$. The result is shown in Figure 4 for CDS images only. A similar procedure was applied to the EIT sequence as well. More details on the analysis of the individual CDS rasters can be found in Paper I. Here we only mention that the rasters were taken by moving the slit from west to east, right to left, in the images of Figure 4, where the beginning of each raster is indicated at the top of the corresponding column.

Step 3. We computed the light curves of the excess irradiance for each spectral feature by summing the contributions $\Delta f_{ij}^k(t_h)$. Each curve represents the contribution of the considered feature to the EUV excess irradiance during the flare, under the assumption that no other significant event is occurring on the solar surface outside the CDS FOV. We verified the correctness of that assumption by inspecting the full-disk EIT 19.5 images during the event. The resulting light curves are shown in the top panel of Figure 5. The set of CDS and EIT curves cover a broad range of temperatures (from $\log T < 5.0$ for He I and He II to $\log T \sim 6.9$ for Fe XIX) and can thus be regarded as a good set of proxies for the temporal and spatial evolution of the various temperature components of the flaring plasma.

Step 4. We found a linear combination of those light curves matching reasonably well the evolution of $\mathrm{SEM}_{[0]}$ measurements during the flare. In more detail, we modeled the total excess irradiance at each time t_h, $\Delta f(t_h)$, with a linear combination of the excess irradiance of each line k in the form

$$\Delta f(t_h) \approx a_0 + a_1 t_h + \sum_k b_k \sum_{ij} \Delta f_{ij}^k(t_h). \qquad (1)$$

The term $a_1 t_h$, which accounts for possible overall changes in the active region structure (hence of the overall EUV emission) in the course of the event, is actually rather small; to reduce the number of free parameters, we set this term to zero.

The two resonance helium lines, He I 58.4 nm and He II 30.4 nm, exhibit an almost identical behavior; only the latter has been taken into account in the linear regression. The comparison of the thus modeled EUV SEM irradiance (Fig. 5, *gray line*) with the actual measured signal (smoothed to account for the 5 minute duration of the CDS rasters) is shown in the bottom panel of Figure 5 for the first ≈120 minutes of the event. We stress that $b_k \sum_{ij} \Delta f_{ij}^k$ is *not* the contribution of the individual line k to the EUV irradiance, but is instead the contribution of the *group* of lines of similar temperatures, for which line k is a proxy.

Beyond the mere application of the mathematical linear regression procedure, we think it useful to remark here that the different parts of the irradiance SEM light curve are due to different temperature contributions of the flare plasma. More specifically, the first peak, at the time resolution of the CDS rasters, is modeled essentially by the cooler temperature lines (the proxies He II and O V), while the second peak (at ∼16:20 UT) is due mostly to the hottest flaring plasma (the proxy Fe XIX), with a tail modeled by progressively cooler components (Fe XVI and then EIT 19.5). These findings, based on the modeling of the $\mathrm{SEM}_{[0]}$ light curve,

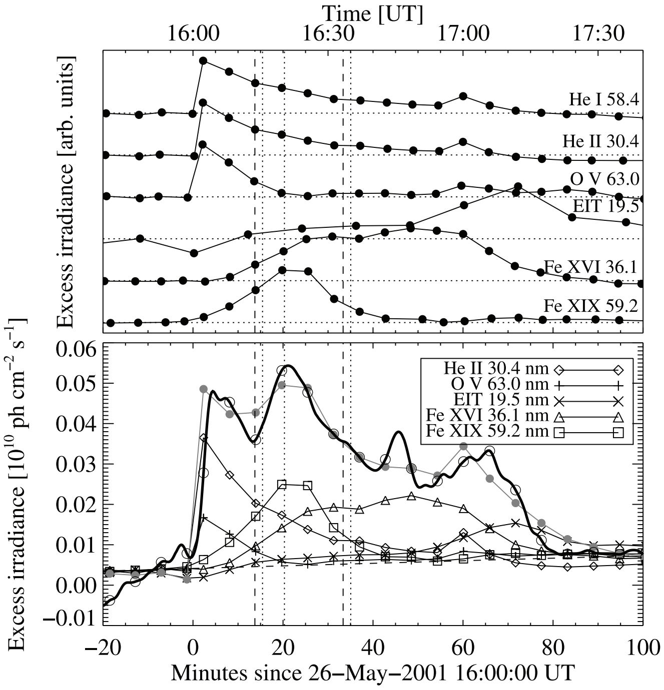

FIG. 5.—*Top*: Light curves of residual irradiances in CDS lines and the EIT enhancement over the flaring region. *Bottom*: Light curve of excess $\mathrm{SEM}_{[0]}$ irradiance during the flare (*thick black line and open circles*), compared with the fit (*gray line and filled circles*) obtained by combining the CDS and EIT light curves. The vertical dashed and dotted lines mark the times of the spectra taken in regions A and D, as in Fig. 2.

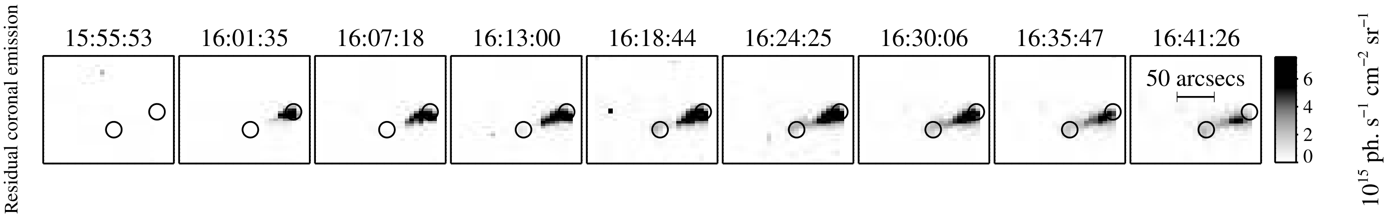

Fig. 6.—Sequences of images showing the variation of the *enhancement* of EUV illumination in the $\lambda < 50$ nm band in the flaring area. Radiance maps are shown with the same format as in Fig. 4.

are qualitatively consistent with the characteristics of the other irradiance curves shown in Figure 2: the second peak is indeed absent in $\mathrm{SEM}_{[1]}$, while it is more pronounced in the *GOES* signal.

Step 5. The coefficients of the linear combination b_k were then applied to the corresponding residual images on a pixel-by-pixel basis, producing a map of the contribution to the total excess EUV irradiance in the SEM spectral range ($\lambda < 50$ nm) as a function of time during the flare. The contribution due to the transition region and coronal lines (henceforth, for brevity, "the coronal component") needed in the model calculations is obtained by subtracting the contribution of the proxy He ii 30.4 nm, which is computed self-consistently in the models. Thus, the contribution of each pixel to the EUV coronal irradiance, divided by the pixel's angular size, yields an estimate of the spatial variation of coronal radiance enhancement in the band $\lambda < 50$ nm over the flare area. The result of such a procedure is shown in Figure 6.

If we make the reasonable assumption that the EUV emission during the flare is optically thin, the maps of EUV excess radiance of Figure 6 are also maps of EUV back-radiation illuminating the chromosphere. In § 3.1 we discuss this assumption in more detail.

Step 6. Finally, by adding the preflare, average value of radiance estimated in the two target regions, A and D, we obtained an estimate of the value of EUV radiance of coronal origin in the band $\lambda < 50$ nm, I_{cor}, as a function of time over the two target regions, and in particular at the times of the optical observations of Figure 3 (Table 1).

The (statistical) uncertainties in the excess number of photons are of the order of $\approx 0.4 \times 10^{15}$ (region A) and $\approx 2 \times 10^{15}$ (region D) photons $\mathrm{s}^{-1}\ \mathrm{cm}^{-2}\ \mathrm{sr}^{-1}$, estimated as the 3 σ variation of the illumination around the target regions. We have also explored the systematic variations induced by changing the most relevant parameters that could affect the result of the procedure described above (for example, using a constant instead of a linear background in the regression calculations of step 4); the resulting overall variations are smaller than the statistical uncertainty at the 3 σ level quoted above. Together with the uncertainty in the preflare radiance enhancements estimated earlier in this section ($\approx$30%) and the uncertainty of I_{ref} estimated in Paper II (0.2×10^{15}, or about 17%), we thus obtain an overall uncertainty in the total coronal radiance of the order of 25% to 35% in both regions A and D.

3.1. *The Spectral and Angular Distribution of the Coronal Back-Radiation*

In Paper II we estimated the spectral distribution of the coronal photoionizing EUV radiation by taking a reference spectral distribution and multiplying that distribution by a factor (close to unity) such that the radiance in the range $\lambda < 50$ nm equals $I_{\mathrm{ref}} = 1.2 \times 10^{15}$ photons $\mathrm{s}^{-1}\ \mathrm{cm}^{-2}\ \mathrm{sr}^{-1}$. In that paper we adopted as our reference spectral distribution the one for a typical active region computed with the spectral code and atomic database CHIANTI, version 4 (Young et al. 2003). The CHIANTI calculations require a description of the density and temperature distribution in the atmosphere via the differential emission measure (DEM), defined as $N_{\mathrm{H}} N_e (dT/dh)^{-1}$, where h is a coordinate along the line of sight; we adopted the table in the file `active_region.dem` provided with the package, which is based on data from Vernazza & Reeves (1978). Furthermore, we adopted a hybrid set of abundances (intermediate between photospheric and coronal elemental mixtures; Fludra & Schmelz 1999) and a constant pressure of $P_e/k = 3 \times 10^{15}\ \mathrm{cm}^{-3}$ K. We verified that the use of the more recent version 5 of the same code (Landi et al. 2006) did not significantly alter that reference spectral distribution (Fig. 1 of Paper II).

In the case of the flaring atmosphere we are considering, however, it is possible that significant changes in the spectral distribution may occur. We tested this possibility by considering the case in which departures from the standard spectral distribution (the preflare AR EUV spectrum, in fact) could be more pronounced, namely, the emission above region D at 16:20 UT, where we observe a peak of total EUV emission (Table 1), as well as a peak in the hot Fe xix line (Fig. 5).

To do so, we found a DEM producing the measured total number of photons in the range $\lambda < 50$ nm (9.2×10^{15} photons s^{-1} $\mathrm{cm}^{-2}\ \mathrm{sr}^{-1}$) that gives at the same time a reasonable match to the transition region and coronal lines observed by CDS: O v 62.9 nm, Fe xvi 36.1 nm, and the blend Fe xii 59.26 + Fe xix 59.22 nm. The optically thick helium lines have not been considered in this analysis, but are nonetheless shown in the plots summarizing the results of this test (Fig. 7).

In the calculations, we assumed a higher pressure, $P_e/k = 3 \times 10^{16}\ \mathrm{cm}^{-3}$ K, than in the preflare atmosphere. This value of the pressure corresponds, for instance, to $N_e \approx 10^{11}$ and $\approx 10^{10}$ at $\log T = 5.5$ and 6.5, respectively. These densities are generally consistent with flare densities found in the literature (e.g., Dere & Cook 1979), although lower densities have sometimes been reported (Cook et al. 1994). Setting aside the overall scale factorized by the DEM, the specific value for P_e/k affects only the relative radiances of the density-dependent lines, and thus it is of little importance for the purpose of estimating the *global* flare spectral distribution for $\lambda < 50$ nm.

Such a DEM is compared in the left-hand panel of Figure 7 with the DEM used to compute the preflare, reference spectrum. The corresponding observed line radiances are shown in that panel multiplied by the factor $\mathrm{DEM}(T_{\mathrm{eff}})/I_{\mathrm{calc}}$ (as in, e.g., Del Zanna et al. 2002); here T_{eff} is the temperature of peak line emission. The error bars in the case of the data taken during the flare reflect the statistical variability in the nine pixels around and above the target region (D). Thus, we do not show the theoretical uncertainties or the calibration uncertainties on either the absolute intensities or the CDS NIS1/NIS2 relative radiances (i.e., the radiance of the Fe xvi line relative to all the others).

The DEM-derived preflare and the flare spectra are compared in the right-hand panel of Figure 7 (*dark and light gray histograms,*

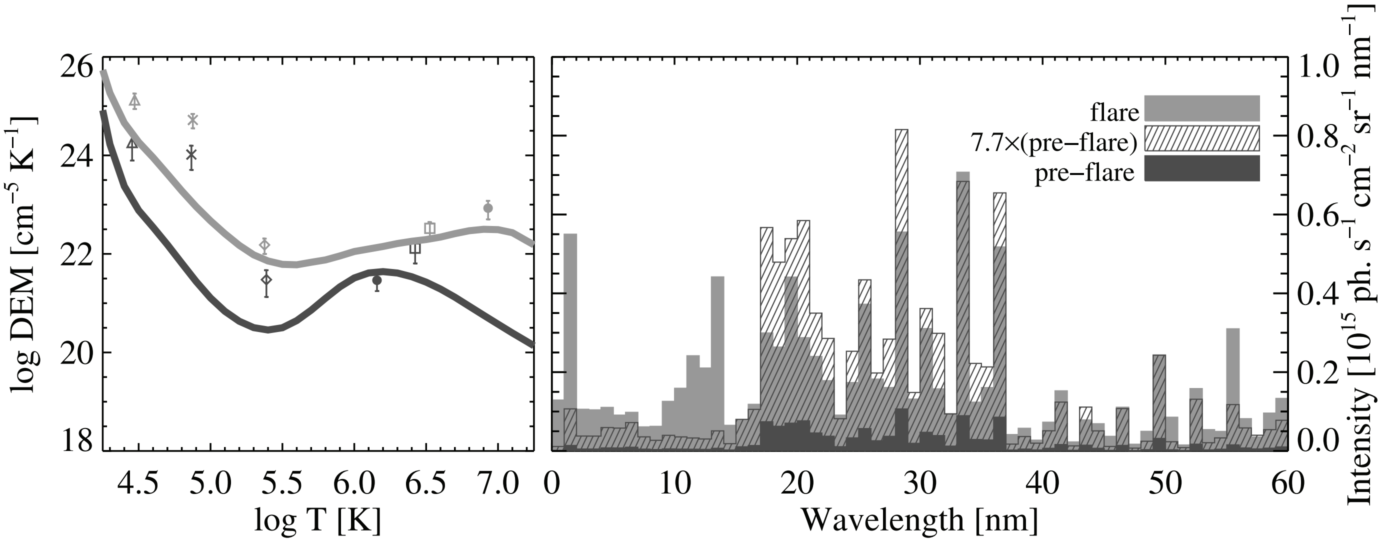

FIG. 7.—*Left*: DEM distributions for the reference AR atmosphere (*black line*) and the flaring region D at 16:20 UT (*gray line*). The observed intensities [multiplied by the factor DEM($T_{\rm eff}$)/$I_{\rm calc}$] are also shown for the various CDS lines: He I 58.4 nm (*triangles*), He II 30.4 nm (*crosses*), O V 62.9 nm (*diamonds*), Fe XVI 36.1 nm (*squares*), and the blend at 59.2 nm (*filled circles*). *Right*: Spectral distributions from the above DEMs, excluding all He I and He II lines and continua, compared with the standard AR emission times the multiplicative factor of ≈7.7 given in Table 1 (*dashed histogram*).

respectively). We also show the preflare standard spectrum multiplied by the factor required to obtain the same total number of photons below 50 nm as in the flare spectrum (*dashed histogram*). The largest differences between these two spectra occur in the region below 15 nm, where the number of photons in the modeled flare spectrum is about a factor of 4 higher than in the AR-scaled spectrum. Conversely, the number of photons in the range 15–50.4 nm is about 20% smaller than in the AR-scaled spectrum.

On the other hand, for both distributions the bulk of the photoionizing photons is in the range 15 nm $< \lambda <$ 50 nm (about 3/4 of the total). In fact, this is the main reason why, as discussed in Paper II, the shorter wavelength part of the spectral distribution has relatively little effect on the photoionization of helium. We found that only the He I 1083 nm line shows small changes, due to the different penetration depths in the chromosphere of the EUV photons of different energies. We further discuss this point in § 5.2.

In conclusion, we expect and indeed find (see § 5.2) that for our calculations it is not necessary to take into account the details of the distribution of photon energies. After all, we are studying a quite small flare. We thus simply scaled the standard spectral distribution by the appropriate factors listed in the last column of Table 1. Concerning the problem of the angular distribution of the EUV photoionizing photons, we have already shown in Paper II that, despite their relatively featureless spatial distribution across the target AR prior to the flare, at the chromospheric depths the details of the angular distribution are relatively unimportant compared to the overall spectral distribution and, most importantly, to the total number of impinging photons.

In the case considered in this paper, on the other hand, during the flare the EUV emission is clearly concentrated in smaller areas (Figs. 4 and 6). It is therefore reasonable to assume that the main sources of ionizing radiation are concentrated directly above or very near the target regions. We verified this assumption using the control region (region A). During the time span we are considering, the helium lines in that region hardly change (Fig. 3), despite the large variations of the EUV radiation around (above) region D (see Table 1), which is roughly 40 Mm away. So, it is clear that the flaring chromosphere in region A, and a fortiori in region D, is sensitive only to the EUV radiation coming from regions significantly closer than 40 Mm ≈50″ or, in other words, is sensitive to the radiation coming at most from a few EIT or CDS pixels away.

4. CHROMOSPHERIC MODELING

Once the coronal back-radiation has been determined, semiempirical models were constructed to match the observed profiles. The modeling was done using the program PANDORA (Avrett & Loeser 1984). Given a T versus h distribution, we solved the non-LTE radiative transfer and the statistical and hydrostatic equilibrium equations and self-consistently computed non-LTE populations for 10 levels of H, 29 of He I, 15 of Fe I, 9 of C I, 8 of Si I, Ca I, and Na I, 6 of Al I and He II, and 7 of Mg I. In addition, we computed 6 levels of Mg II and 5 of Ca II. The atomic models we used for H and Ca II are described in Mauas et al. (1997) and Falchi & Mauas (1998). The models we used for He I and He II are described in Paper II. More details on the modeling and the different assumptions and their validity can be found in Falchi & Mauas (1998) and in Paper II. The adopted microturbulence, in particular, is the same as in the latter work.

The modeling was done in a plane-parallel atmosphere. This is certainly an adequate approximation if we consider the much larger horizontal size of the target areas (several thousands of km) compared with the thickness of the chromosphere under study (a few hundred km). The effect of a possible filamentary structure of the atmosphere is, however, much more difficult to assess.

The only (qualitative) assessment we can make, from a radiative transfer point of view, is that photons could perhaps escape more easily from a set of randomly oriented, high-density structures embedded in a lower density medium than from a homogeneous atmosphere, especially in the case of high-density contrast and of a sparse distribution of the filamentary structures. Thus, we may expect some modifications in the details of the profiles of the more optically thick lines, for instance, a reduction of the depth of self-reversed cores, if present. We may also expect that (effectively) optically thin lines should be least affected by atmospheric inhomogeneities.

In the case of more ordered, more closely packed, and thicker structures, on the other hand, the outcome could be somewhat different, as shown by Gunár et al. (2007), who studied the formation

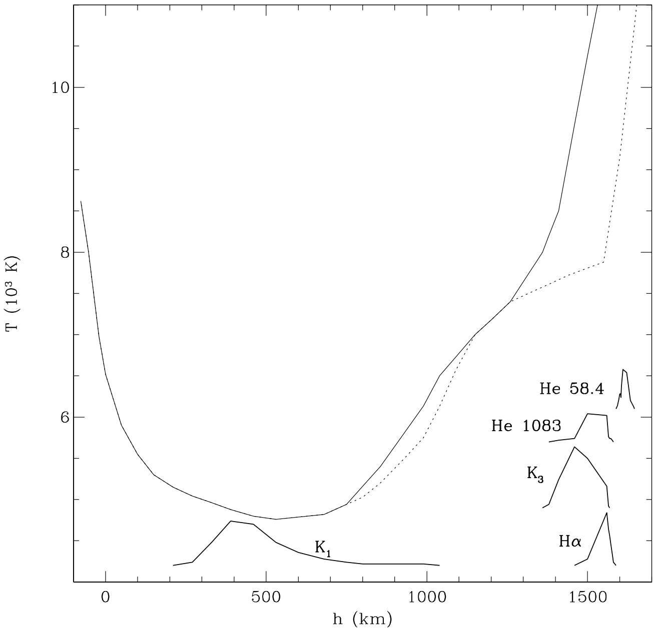

FIG. 8.—Region A: temperature vs. height distribution (*solid line*) of the atmospheric model obtained for $A_{\rm He} = 0.1$. The model for the active region studied in Paper II (*dotted line*) is displayed for comparison. Also shown are the intensity contribution functions, in arbitrary units (*thick solid lines*), of the different spectral features we used to build the model. The He I 587.6 nm contribution function is proportional to the one for the infrared He I line.

of the hydrogen Lyman lines in prominences, modeled as a set of parallel, finite slabs (threads), each 1000 km wide, each one, that is, as wide as the entire chromosphere we are modeling (Figs. 8 and 11). We remark, however, that even in such a relatively extreme case, the changes are typically not very dramatic and are observable only at high spectral resolution.

In any case, there is little or no information, to our knowledge, on the effect of a flare on the chromospheric fine structure. Thus, any more precise assessment of the effect of nonuniformity on the emerging profiles is virtually impossible at this stage.

In Figure 3 we have shown the sets of optical profiles used in the modeling procedure. Since different features of the lines are sensitive to modifications in different parts of the chromosphere, the models were constructed following several steps. First, we fixed the deepest part of the atmosphere by matching the wings and the K_1 minimum of the Ca II K line, which are formed in the high photosphere and the temperature-minimum region.

As a second step, we modified the chromosphere and the lowest part of the transition region until a satisfactory match was found for the profiles of Hα, Ca II K, and He I 1083 nm and 587.6 nm. We recall that the profiles of the first two lines do not depend on the coronal back-radiation field.

The profiles of the two helium lines are formed in two distinct regions; most of the radiation originates in the photosphere, which in the quiet Sun results in a weak absorption line at 1083 nm and no noticeable line at 587 nm. However, in the active region studied in Paper II we already found that there is an important chromospheric contribution. This contribution becomes, of course, much more important in the flaring atmospheres we are studying here and depends not only on the thermal structure of the high chromosphere and the low-transition region, between 10^4 and 2.5×10^4 K, but also on the coronal EUV incident radiation.

Finally, both ultraviolet lines, the He I line at 58.4 nm and the He II line at 30.4 nm, depend on the structure of the low- and midtransition region, from 3×10^4 to 5×10^4 K for the 58.4 nm line and up to 1×10^5 K for the 30.4 nm line. As a third step, therefore, we modified the structure of this region to obtain a good match for the line fluxes of these UV lines, measured with *SOHO* CDS. Generally, it was necessary to iterate between steps 2 and 3 before a final model was obtained.

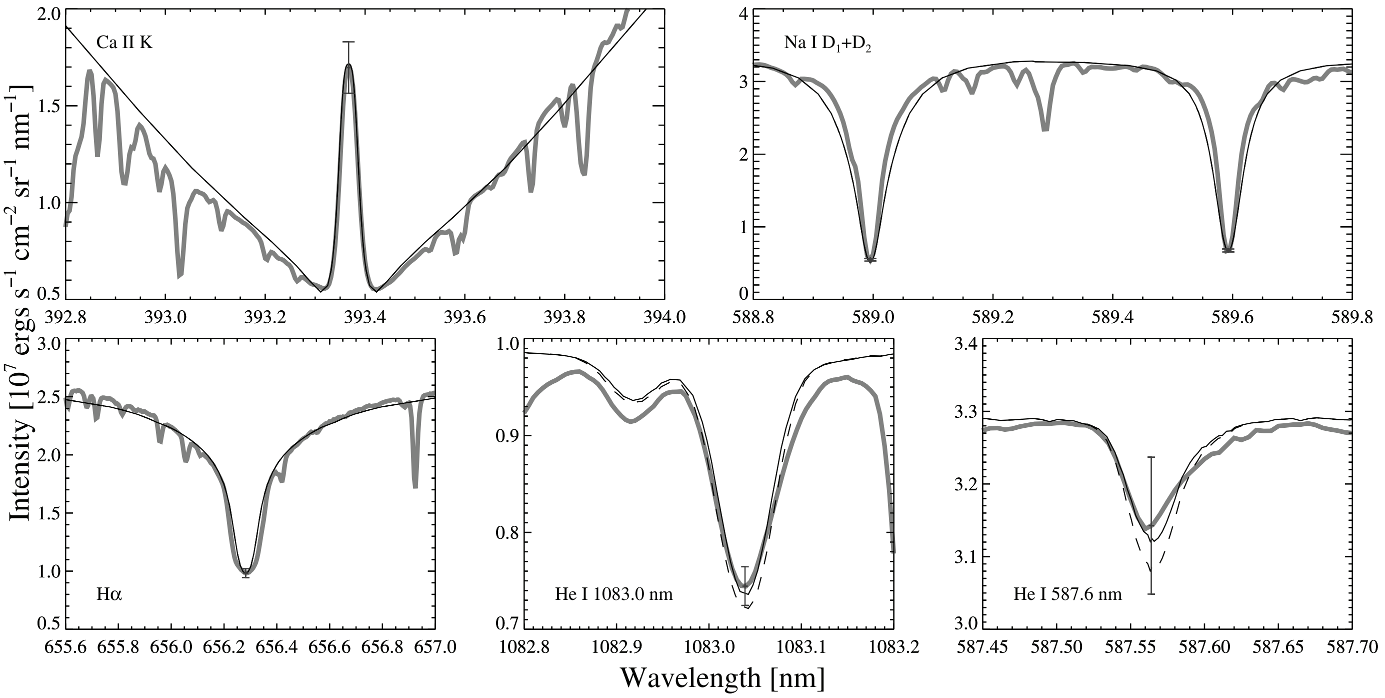

FIG. 9.—Region A: comparison between observed (*thick gray line*) and computed profiles (*black lines*). The solid and dashed lines indicate the profiles computed for the radiation determined at 16:14 and 16:33 UT, respectively.

TABLE 2

Observed and Computed Radiances for the He UV Lines

Time (UT)	He I 58.4 nm Observed	He I 58.4 nm Computed	He II 30.4 nm Observed	He II 30.4 nm Computed
Region A				
16:14	2.65	2.77	16.0	15.3
16:33	2.65	2.91	16.0	14.0
Region D				
16:15	4.34	4.35	32.7	31.5
16:20	4.93	5.29	24.0	22.9
16:35	3.24	3.32	14.6	15.4

Note.—Units are 10^4 ergs s^{-1} cm^{-2} sr^{-1}.

We first computed models for regions A and D, marked in Figure 1, using the coronal radiation determined in § 3 and the same value of the helium abundance ($A_{\rm He} = 0.1$) that we used in Paper II. The resulting computed intensity profiles were convolved with the appropriate instrumental response.

4.1. *Modeling of Region A*

For region A, where the observed lines do not change during the time interval that we considered, we obtained the model shown in Figure 8, which gives a good match between the observed and computed lines. In the same figure, we also show, for the line cores, the intensity contribution functions, defined as $dI/dh = S \exp(-\tau)\chi$, where I is the intensity, h is the height in the atmosphere, and S, τ, and χ are, respectively, the source function, the optical depth, and the opacity in the line core.

The observed and computed profiles of the lines formed essentially at chromospheric levels are shown in Figure 9. The bars in the figure indicate the uncertainty of the observed profiles (see also Fig. 3). It can be seen that the agreement found is very good, well within the error bars, in all cases. In the case of the optical He I lines, however, we recall that, as discussed in § 2, the error bars in the line centers also include the effect of variations of the underlying photosphere within the target region and therefore represent an upper limit to the variation induced by chromospheric changes. It can also be seen that only the He lines are affected by the EUV radiation and that the computed profiles agree with the observations within the range of variability in the target region for both values of the coronal radiation indicated in Table 1.

We have already mentioned in § 2 that the UV lines (the He I 58.4 nm and the He II 30.4 nm lines) have a large width due essentially to the instrumental profile; therefore the comparison with the models can be done only through the radiances, which are shown in Table 2. It can be seen that it is possible to obtain line radiances in good agreement with the observed ones using the same atmosphere, despite the variation of the coronal radiation of about 50% during the time interval we considered (see § 3; Table 1).

We remark here that the temperature structure in the region of formation of the He II 30.4 nm line is not constrained by other lines. Thus, for the remainder of the discussion, we do not consider a match of the He II Lyα to be a significant constraint on the atmospheric parameters.

4.2. *Modeling of Region D*

For region D, where the chromospheric intensity (Fig. 2) approximately follows the EUV light curves, we were able to find models reasonably matching the observations at t_1 and t_3, but it was not possible to obtain a model that would simultaneously reproduce all the profiles observed at t_2. In particular, the radiances of the He I 58.4 nm line always result considerably higher than the observed one if we match the profiles of the other lines, in particular Hα. Conversely, it is possible to find models that reproduce the radiance of the resonance He I line, but in this case the other lines, in particular Hα, are poorly fitted. It should be kept in mind that it is precisely at this time that the regions of formation of the 58.4 nm line and of Hα overlap most, and therefore the model is best determined (see § 5.1).

5. DISCUSSION

In order to find in region D a model of the flaring atmosphere that matches all the observed lines during the considered time interval and in particular that matches *both* Hα *and* He I 58.4 nm, we explored the two aspects that most likely affect the helium spectrum, the chromospheric helium abundance, $A_{\rm He}$ (§ 5.1) and the spectral distribution and overall level of EUV coronal back-illumination (§ 5.2).

5.1. *The Effect of Helium Abundance*

To explore the effect of the helium chromospheric abundance, we computed a series of models for kernel D at t_2 using values of $A_{\rm He} = 0.085$, 0.075, 0.065, and 0.055 for $T > 6300$ K, i.e., in the atmospheric layers that strongly contribute to the formation of the considered lines. Since a change in the helium abundance affects the hydrostatic equilibrium, models with the same T versus h structure but different abundances give, in principle, different emitted profiles, not only for the He lines, but for all the other chromospheric lines as well, and for Hα and the Ca II lines in particular. Therefore, for each value of $A_{\rm He}$ we had to compute a different model.

In Figure 10 we show the computed radiance of the 58.4 mn He line and the central intensity of the D_3, 1083 nm, and Ca II K lines, for the best-matching models for every value of the assumed $A_{\rm He}$. The observed values and their uncertainties, as described in § 2, are also shown. The variations of Hα around the mean value of its central intensity are of the same order as the analogous variations of the Ca II K line and thus are not shown in Figure 10.

The Ca II K and the He I 1083 nm lines depend very weakly on $A_{\rm He}$, in the sense that, for each value of $A_{\rm He}$, it was possible to find a model matching the observed profiles within the errors. On the contrary, the He I D_3 and 58.4 nm lines strongly depend on $A_{\rm He}$: the 58.4 nm radiance is higher than the observed value (beyond the error bar) for $A_{\rm He} = 0.1$ and quickly decreases for smaller values of $A_{\rm He}$, crossing the mean observed value at $A_{\rm He} \sim 0.07$. On the other hand, the D_3 central intensity increases with decreasing $A_{\rm He}$ and for $A_{\rm He}$ smaller than $\sim$0.075 significantly exceeds the observed value. In practice, the D_3 central intensity approaches the photospheric continuum; i.e., the line *disappears* for $A_{\rm He} < 0.05$.

In other words, both the He I D_3 and 58.4 nm lines become in fact *weaker* as $A_{\rm He}$ decreases. This result may appear obvious after a superficial analysis neglecting the nonlinearity of non-LTE problems. In fact, the He I 1083 nm line does not display the same behavior; over the range of abundances explored, it was nearly always possible to find a temperature structure fitting both that line and the other chromospheric lines—with the exception of the lowest value, $A_{\rm He} = 0.05$.

Considering the error of the measurements, we believe that $A_{\rm He} = 0.075$ is the best compromise that allows reasonably good

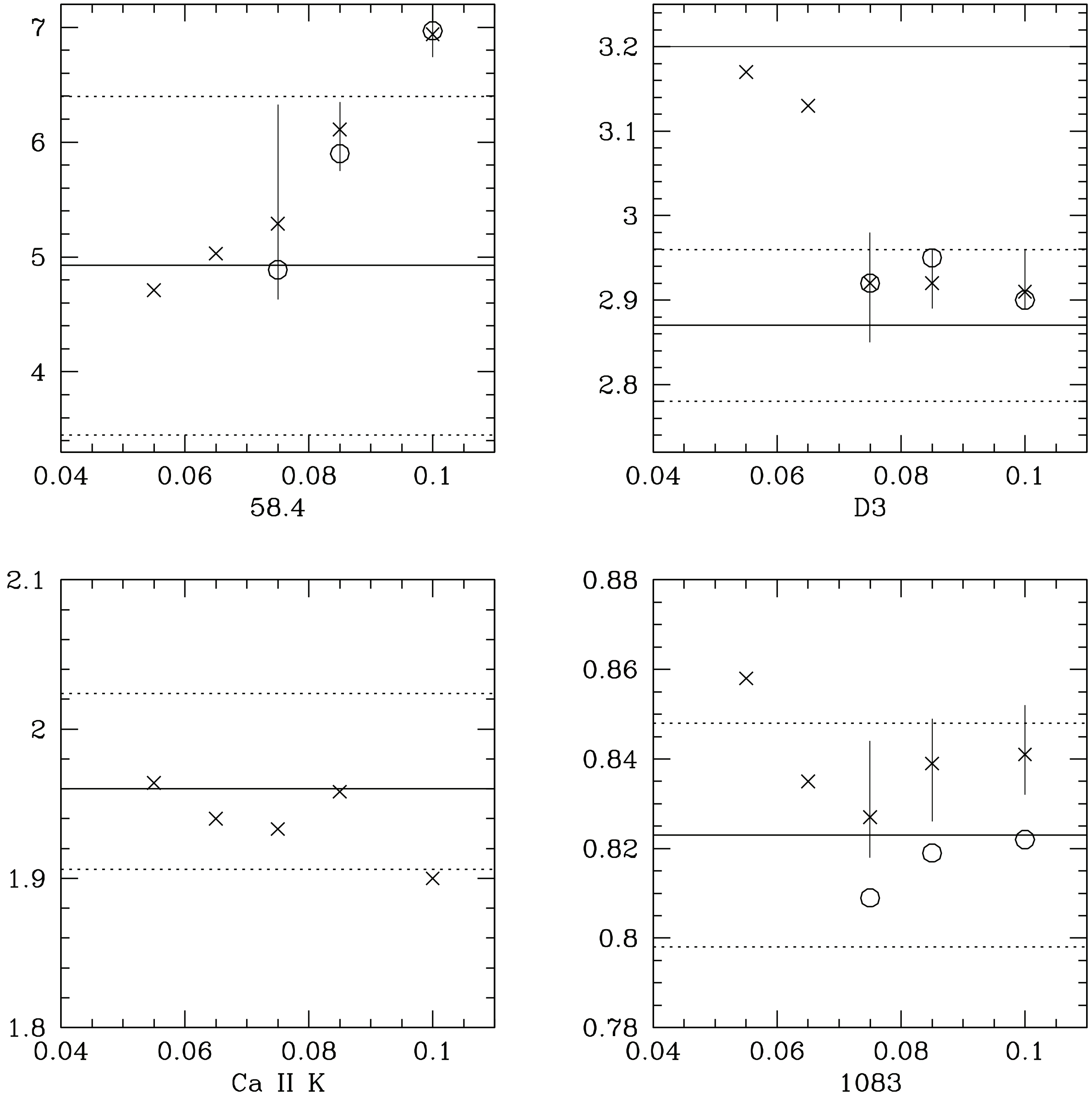

Fig. 10.—Computed radiance (10^4 ergs s^{-1} cm^{-2} sr^{-1}) and central line intensity (10^7 ergs s^{-1} cm^{-2} sr^{-1} nm^{-1}) vs. $A_{\rm He}$. The radiance of the 58.4 nm line and the line center intensity of the D_3, 1083 nm, and Ca II K lines are computed for the best-matching models obtained for region D at t_2, with $I_{\rm cor}$ given in Table 1 and the scaled spectral distribution of the active region (*crosses*). Open circles indicate values obtained with the flare spectral distribution described in § 3.1. The thick line indicates the observed value and the dotted line its estimated uncertainty. The thin line indicates the continuum level for D_3.

matches for all the considered lines. We note that a variation of ±14% of $A_{\rm He}$ (i.e., $0.65 \leq A_{\rm He} \leq 0.85$) still allows a good match between observed and computed lines within the error of the observations. With this value of $A_{\rm He}$, we also determined the models for region D at t_1 and t_3 UT, which are shown in Figure 11. The same figure also shows for the line cores the intensity contribution functions for the model corresponding to the second maximum of EUV emission, at t_2.

A comparison between observations and calculations for the three models is shown in Figure 12. The bars in the figure indicate the uncertainties of the observed profiles. It can be seen that the agreement found is very good, well within the errors, with the same caveat regarding the error bars of the optical He I lines discussed in § 4.1. The computed radiances for the UV lines are compared with the observation in Table 2. Also in this case, the agreement is well within the errors in the observations.

5.2. *The Effect of Coronal Illumination*

In the discussion on the effect of $A_{\rm He}$ on our calculations, we have assumed the values of $I_{\rm cor}$ given in Table 1. Those values,

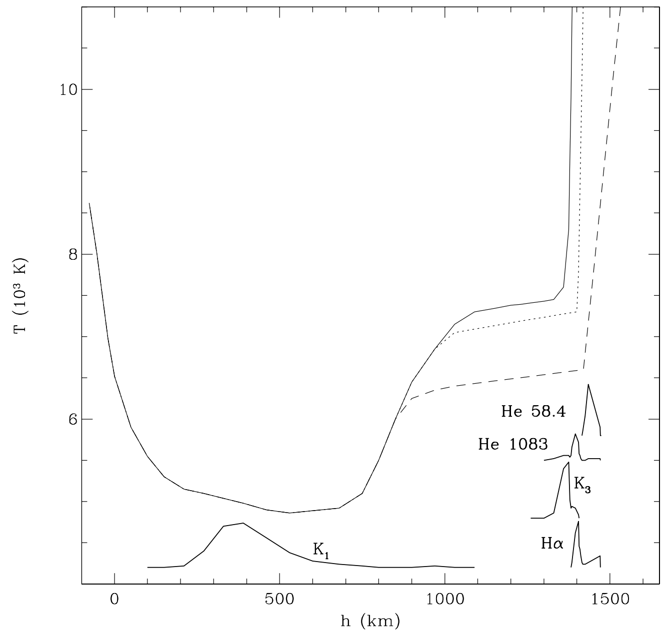

FIG. 11.—Region D: temperature vs. height distribution of the atmospheric models obtained for $A_{\rm He} = 0.075$ at the considered times (*dotted line*: 16:15 UT; *solid line*: 16:20 UT; *dashed line*: 16:35 UT). Central intensity contribution functions of various lines are also shown, as in Fig. 8.

however, have an uncertainty of about 30%, as estimated in § 3. Moreover, the spectral distribution of the photoionizing photons is also somewhat uncertain. To assess how these uncertainties affect the profiles of the helium lines, we performed a set of calculations for kernel D at t_2, since it corresponds to the second emission peak (after the initial impulsive peak), when the differences with the situation studied in Paper II are the largest.

To test the effect of the uncertainty in the overall coronal back-illumination, we computed the He profiles, increasing and decreasing by the $\approx$30% estimated uncertainty (§ 3) the value listed in Table 1 for the models with $A_{\rm He} = 0.1$, 0.085, 0.075. The results of this tests are synthetically shown in Figure 10 by thin error bars: higher values of $I_{\rm cor}$ produce stronger He I lines (deeper optical lines and higher radiances in the EUV line).

For $A_{\rm He} = 0.1$, we found that the computed radiances of the He I 58.4 nm line change very little. In fact, a change in $I_{\rm cor}$ much larger than 30% (which, we recall, is a safe 3 σ value) would be required to match this radiance within the error bar of the observed value.

For $A_{\rm He} = 0.075$, for which we obtained the best overall fit (§ 5.1), we found that modifying the value of $I_{\rm cor}$ by 30% does indeed produce significant changes in the calculated profiles. It appears in this case that the lower value of $A_{\rm He}$ increases the penetration depth of EUV coronal photons, toward regions where the P-R mechanism effectively competes with collisional processes in the formation of the helium spectrum, even of the EUV resonance He I line.

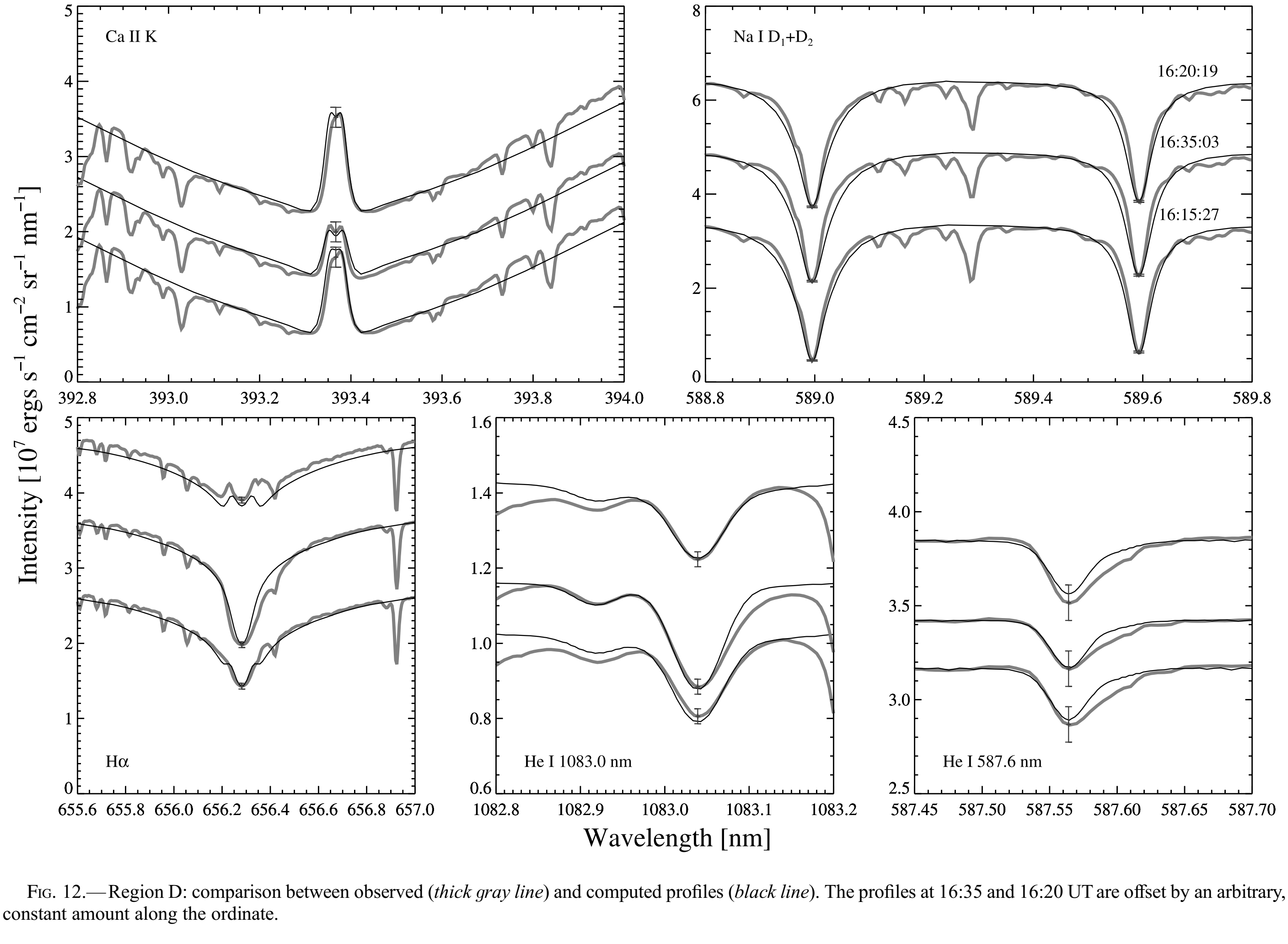

FIG. 12.—Region D: comparison between observed (*thick gray line*) and computed profiles (*black line*). The profiles at 16:35 and 16:20 UT are offset by an arbitrary, constant amount along the ordinate.

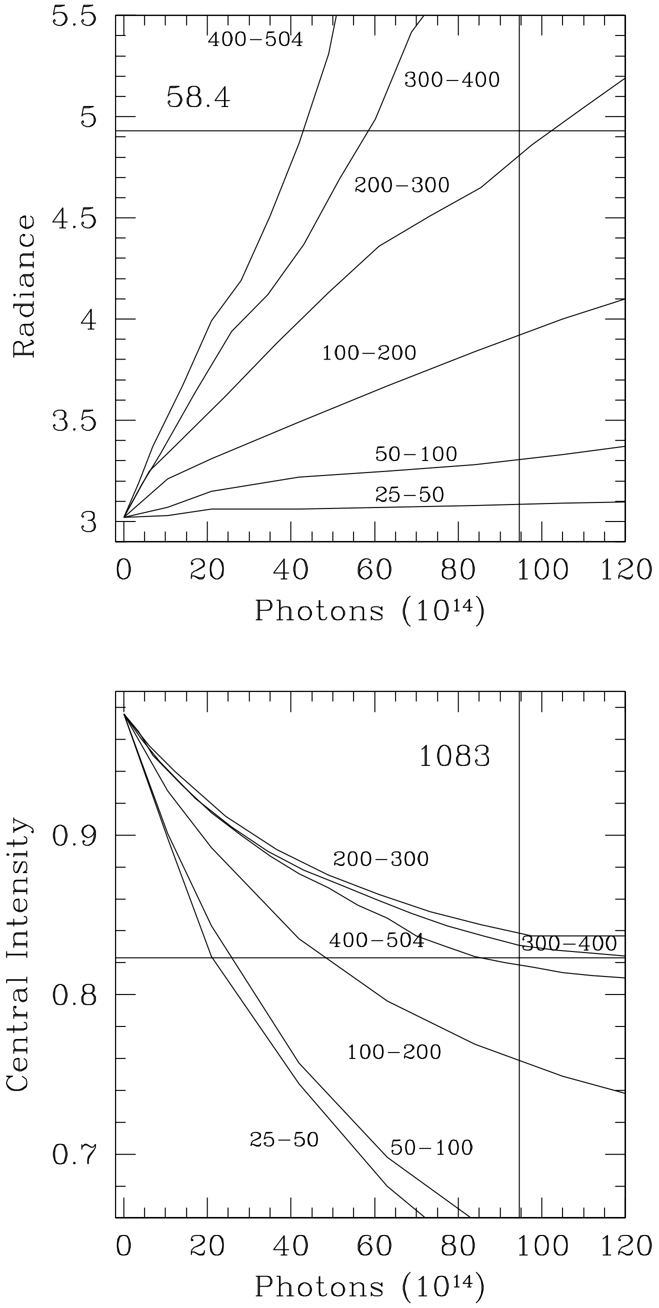

Fig. 13.—Radiance for the 58.4 nm line (*top*) and central intensity of the 1083 nm line (*bottom*), as a function of $I_{\rm cor}$ for different steplike distributions of the field. Units are the same as in Fig. 10 for the ordinates, $I_{\rm cor}$, given in 10^{14} photons $\rm s^{-1}$ $\rm cm^{-2}$ $\rm sr^{-1}$. The vertical line marks the value of $I_{\rm cor}$ at t_2, while the horizontal lines indicate the mean value of the measured 58.4 nm radiance (*top*) and 1083 nm central intensity (*bottom*).

To assess to what extent the uncertainty in the spectral distribution of EUV coronal photons can affect the results described in § 5.1, we computed the He i profiles using the DEM-derived flare spectral distribution described in § 3.1, for the cases with $A_{\rm He} = 0.1$, 0.085, and 0.075. The results are indicated in Figure 10 with open circles. It can be seen that the changes are small, well within the error of the observations. We can therefore exclude that the discrepancy between calculations and observations in the case of $A_{\rm He} = 0.1$, noted in § 4.2, can be due to the uncertainty in the photoionization radiation.

In order to explore more systematically the effect of the spectral distribution of the photoionizing radiation, we also performed tests similar to the ones included in Paper II, considering the spectral distribution different step functions, which are nonzero only in a limited spectral range and zero outside it. The wavelength ranges we considered for these tests are 2.5–5.0 nm, 5–10 nm, 10–20 nm, 20–30 nm, 30–40 nm, and 40–50.4 nm.

In Figure 13 we show the intensity in the center of the 1083 nm line and the radiance of the 58.4 nm line as a function of $I_{\rm cor}$. We do not show the central intensity of the D_3 line, since its behavior is very similar to the one of the 1083 nm line. We note that in Paper II we limited our tests to EUV radiances $I_{\rm cor} < 3 \times 10^{15}$ photons $\rm s^{-1}$ $\rm cm^{-2}$ $\rm sr^{-1}$, whereas here we extended the tests to 1.2×10^{16}.

Several important conclusions can be drawn from this figure. First, the effect is different on the two lines: the central intensity of the 1083 nm line is most sensitive to the harder extreme of the spectrum (down to the threshold of 2.5 nm), while the reverse is true for the radiance of the 58.4 nm line, which is dominated by the longer wavelength bands and is also nearly insensitive to photons below 10 nm. For the 1083 nm and the D_3 lines the relevant parameter, as in the case discussed in Paper II, is the ratio between the helium and hydrogen photoionization cross sections, which in the band 0.5–10 nm is 3–5 times larger than at 50 nm. Therefore, coronal photons at larger wavelengths are absorbed before they reach the chromospheric heights, where these lines are formed. Since, as we explained in Paper II, the ratio between the He i and H cross sections changes slowly at long wavelengths, the details of the spectral distribution between 20 and 50.4 nm are of little relevance for the resulting 1083 nm central intensity.

While these results are qualitatively consistent with those of Paper II, the effect of the shortest wavelength photons (in the band 2.5–5.0 nm) is remarkably different. While that band had practically no effect on the He i 1083 nm line computed in the AR model discussed in Paper II, we found that, in this flaring atmosphere, these photons may have a role in the formation of that line. The reason for the difference lies in the higher temperature and densities of the model chromosphere of region D: the He i 1083 nm line forms in a region where most neutral or singly ionized metals, whose inner shell absorption cross sections would otherwise dominate the opacity in that band, have already mostly disappeared.

The He i 58.4 nm line, on the other hand, is formed higher in the transition region, where most hydrogen is ionized, and therefore in this case the relevant parameter is the helium photoionization cross section alone, which is larger close to the continuum head, at 50.4 nm. Note that, by contrast with the situation studied in Paper II, in this case the much larger coronal radiation has some effect on the radiance of the He i UV line, for $A_{\rm He}$ up to 0.1 (Fig. 10). The He ii UV line, on the other hand, which forms at higher temperatures, is not affected by the coronal radiation, as was the case for the active region prior to the flare (see Paper II).

6. CONCLUSIONS

During a small two-ribbon flare, we obtained simultaneous and cospatial observations, including the chromospheric lines Ca ii K, Hα, and Na i D, as well as the He i lines at 587.6 nm (D_3), 1083 nm, and 58.4 nm and the He ii line at 30.4 nm. The EUV irradiance in the ranges $\lambda < 50$ nm and 26 nm $< \lambda < 34$ nm was also measured at the same time.

We analyzed the formation of the He lines after the first impulsive burst of the flare, i.e., after 16:13 UT, in two different locations of the flaring area, named A and D. In region A the chromospheric radiance is almost constant during the time interval we considered, while in region D it approximately follows the EUV light curve with a maximum emission at about 16:20 UT (Fig. 2). A similar behavior is also detected for the TR and coronal lines with temperatures up to 10^6 K. We determined the incident photoionizing EUV radiation produced by the corona overlying the target regions by using information from various *SOHO* instruments (imagers and spectrographs), and we concluded that in region A the variability of coronal radiance during the flare is less than a factor of 2, while in region D it is about a factor of 5 (Table 1).

We determined the spectral distribution of the coronal radiation over the region D at 16:20 UT, where we observe a peak of total EUV emission, as well as a peak in the hot Fe XIX line (Fig. 5). We found that the largest differences between the preflare and the flare spectrum occur in the region below 15 nm.

These differences, however, are not large enough to compensate for the overwhelming contribution of longer wavelength photons to the total EUV photoionizing emission in this relatively small flare. We therefore simply scaled the spectral distribution of a typical active region by the appropriate factors listed in the last column of Table 1. With this coronal radiation, we built semiempirical atmospheric models, trying to match our set of observables for regions A and D and using the same value of the helium abundance ($A_{\rm He} = 0.1$) that we used in Paper II. The He lines and continua are self-consistently computed in the radiative transfer calculations.

For region A we were successful in obtaining line spectral intensities and radiances in good agreement, within the errors, with the observed ones at the considered times, using a constant atmosphere and the coronal radiations determined in § 3. Taking into account that the formation of the helium lines in this case still falls in a regime where the P-R mechanism is important (Fig. 9), this result makes us confident that our assumptions for the coronal radiation and its spectral distribution are acceptable.

For region D, we were able to find models producing profiles reasonably matching the observations at 16:15 and 16:35, but it was not possible to obtain a model capable of simultaneously reproducing all the profiles observed at 16:20, when the flare emission is maximum. In particular, it was not possible to simultaneously match Hα and the He I 58.4 nm line. We therefore explored the two aspects that most likely can have an effect on our calculations: the chromospheric helium abundance, $A_{\rm He}$ (§ 5.1), and the spectral distribution and overall level of EUV coronal back-illumination (§ 5.2).

Since a change in the helium abundance affects the hydrostatic equilibrium, for each considered value of $A_{\rm He}$ we had to compute a different model. We used values of $A_{\rm He} = 0.085$, 0.075, 0.065, and 0.055 for $T > 6300$ K, and we showed that the He I D_3 and 58.4 nm lines strongly depend on $A_{\rm He}$, both becoming weaker as $A_{\rm He}$ decreases. In particular the D_3 line disappears for $A_{\rm He} < 0.05$, setting a lower limit for the $A_{\rm He}$ value. On the contrary, over the range of abundances explored, it was always possible to find an atmospheric structure matching He I 1083 nm and the other chromospheric lines. Taking into account the error of the measured lines, we regard $A_{\rm He} = 0.075$ as the best compromise that allows reasonably good matches for all the considered lines, and we found that a variation of ±0.010 (or ±14%) of $A_{\rm He}$ is still acceptable within the error of the observations, *with the average value of coronal illumination determined in* § 5.2.

On the other hand, an analysis of the effect of the coronal illumination *at a given value of* $A_{\rm He}$ (in § 5.2 we considered $A_{\rm He} = 0.1$, 0.085, and 0.075) led us to exclude that uncertainties in the determination of this parameter could be responsible for the discrepancies at $A_{\rm He} = 0.1$. We also determined new models for region D at 16:15 and 16:35 UT using $A_{\rm He} = 0.075$. Thus, for these two times we have models matching all the observations for both $A_{\rm He} = 0.075$ and 0.1. In these cases, as in region A (§ 4.1), the incomplete overlap between the formation regions of Hα and He I 58.4 nm (see, for instance, Fig. 8) does not allow a determination of $A_{\rm He}$ with an uncertainty better than a factor of 2, as in Paper II.

In summary, our analysis of the observed chromospheric spectra is consistent with $A_{\rm He} = 0.075$; furthermore, we were able to estimate the uncertainty range as 0.065–0.085 in at least one favorable case. The value $A_{\rm He} = 0.085$, i.e., the canonical photospheric helium abundance (e.g., Asplund et al. 2005), could therefore be marginally consistent with our data, since it results in He features that agree with the observations at the limit of our estimated errors.

A final note on measuring the helium abundance in the solar chromosphere: The set of lines we have used, together with an estimate of the EUV coronal back-radiation, is the *minimum necessary* to estimate $A_{\rm He}$ in the chromosphere. No meaningful estimates, for instance, can be obtained using only the optical He I lines or the EUV resonance lines alone. But (as in Paper II, or in all cases considered here, except region D at 16:20 UT) even this set of lines may not be *sufficient* for an accurate determination of $A_{\rm He}$. In particular, while the optical He I lines are usually well constrained by typical chromospheric lines such as Ca II K or Hα, the resonance He I 58.4 nm line must also be constrained by lines forming in the lower transition region. In the high-pressure environment of region D at the secondary peak of the EUV flare emission, this role is played by Hα. In other circumstances, additional constraints provided by other lines would be needed: intensities from other upper chromospheric or lower TR lines (e.g., H I Lyα), intensities from other He I and He II lines (e.g., He II 25.6 nm), or spectrally resolved profiles of the He I 58.4 nm and He II 30.4 nm lines. With the advent of more recent space missions, such as *Hinode* and its EUV spectrometer (EIS), and with the continued availability of the *SOHO* spectrometers (CDS and SUMER), there is now in fact a window of opportunity for obtaining stronger constraints for the kind of modeling described in this work.

This work was supported in part by a joint project of CNR (Consiglio Nazionale delle Ricerche, Italy) and CONICET (Consejo Nacional de Investigaciones Cientificas y Técnicas, Argentina). V. A. also acknowledges support from the Italian Space Agency (ASI), contracts ASI/INAF I/035/05/0 and I/015/07/0. We would like to thank the *SOHO* CDS and NSO teams for their support in carrying out the observations analyzed in this paper. We are also grateful to R. Falciani and G. Cauzzi, who acquired the data at NSO. *SOHO* is a project of international cooperation between ESA and NASA. The NSO (National Solar Observatory, US) is operated by the Association of Universities for Research in Astronomy, Inc. (AURA), under cooperative agreement with the National Science Foundation. Finally, we thankfully acknowledge the efforts of the CHIANTI consortium members for making readily available and usable a fine code and database for astrophysical applications. CHIANTI is a collaborative project involving the NRL (Naval Research Laboratory, US), RAL (Rutherford Appleton Laboratory, UK), MSSL (Mullard Space Science Laboratory, UK), the Universities of Florence (Italy) and Cambridge (UK), and George Mason University (US).

REFERENCES

Andretta, V., Del Zanna, G., & Jordan, S. D. 2003, A&A, 400, 737
Andretta, V., & Jones, H. P. 1997, ApJ, 489, 375
Asplund, M., Grevesse, N., & Sauval, A. J. 2005, in ASP Conf Ser. 336, Cosmic Abundances as Records of Stellar Evolution and Nucleosynthesis, ed. T. G. Barnes III & F. N. Bash (San Francisco: ASP), 25
Avrett, E. H., & Loeser, R. 1984, in Methods in Radiative Transfer, ed. W. Kalkofen (Cambridge: Cambridge Univ. Press), 341
Cook, J. W., Keenan, F. P., Harra, L. K., & Tayal, S. S. 1994, ApJ, 429, 924
Del Zanna, G., Landini, M., & Mason, H. E. 2002, A&A, 385, 968
Delaboudinière, J.-P., et al. 1995, Sol. Phys., 162, 291
Dere, K. P., & Cook, J. W. 1979, ApJ, 229, 772
Drake, J. J. 2003, Adv. Space Res., 32, 945
Falchi, A., & Mauas, P. J. D. 1998, A&A, 336, 281
Feldman, U., Landi, E., & Laming, J. M. 2005, ApJ, 619, 1142
Fludra, A., & Schmelz, J. T. 1999, A&A, 348, 286
Fredvik, T., & Maltby, P. 1999, Sol. Phys., 184, 113
Geiss, J. 1982, Space Sci. Rev., 33, 201
———. 1998, Space Sci. Rev., 85, 241
Gunár, S., Heinzel, P., Schmieder, B., Schwartz, P., & Anzer, U. 2007, A&A, 472, 929
Harrison, R. A., et al. 1995, Sol. Phys., 162, 233
Hovestadt, D., et al. 1995, Sol. Phys., 162, 441
Killie, M. A., Lie-Svendsen, Ø., & Leer, E. 2005, ApJ, 632, L155
Landi, E., Del Zanna, G., Young, P. R., Dere, K. P., Mason, H. E., & Landini, M. 2006, ApJS, 162, 261
Mandzhavidze, N., Ramaty, R., & Kozlovsky, B. 1997, ApJ, 489, L99
———. 1999, ApJ, 518, 918
Mauas, P. J. D., Andretta, V., Falchi, A., Falciani, R., Teriaca, L., & Cauzzi, G. 2005, ApJ, 619, 604 (Paper II)
Mauas, P. J. D., Falchi, A., Pasquini, L., & Pallavicini, R. 1997, A&A, 326, 249
Murphy, R. J. 2007, Space Sci. Rev., 130, 127
Pietarila, A., & Judge, P. G. 2004, ApJ, 606, 1239
Share, G. H., & Murphy, R. J. 1998, ApJ, 508, 876
Teriaca, L., Falchi, A., Cauzzi, G., Falciani, R., Smaldone, L. A., & Andretta, V. 2003, ApJ, 588, 596 (Paper I)
Vernazza, J. E., & Reeves, E. M. 1978, ApJS, 37, 485
Young, P. R., Del Zanna, G., Landi, E., Dere, K. P., Mason, H. E., & Landini, M. 2003, ApJS, 144, 135
Zirin, H. 1975, ApJ, 199, L63